



# Catalytic removal of gaseous HCBz on Cu doped OMS: Effect of Cu location on catalytic performance

Yang Yang, Jun Huang, Shuzhen Zhang, Siwen Wang, Shubo Deng, Bin Wang, Gang Yu\*

POPs Research Center, School of Environment, State Key Joint Laboratory of Environment Simulation and Pollution Control, Tsinghua University, Beijing 100084, China

## ARTICLE INFO

### Article history:

Received 9 August 2013

Received in revised form

22 November 2013

Accepted 23 November 2013

Available online 12 December 2013

### Keywords:

Octahedral molecular sieves

Catalytic destruction

Hexachlorobenzene

Persistent organic pollutants

## ABSTRACT

Hexachlorobenzene (HCBz) is a persistent organic pollutant emitted unintentionally from the flue gas of combustion and industrial processes. In this study, copper doped manganese oxide octahedral molecular sieve (Cu-OMS) was synthesized by one-step hydrothermal method and applied for the catalytic removal of low concentration gaseous HCBz. Physicochemical characterization indicates that Cu location within OMS is affected by the precursor Cu/Mn molar ratio ( $\text{Cu/Mn}_{\text{pre}}$ ). Activity tests further show that the catalytic performance of Cu-OMS is associated with Cu location. At low Cu doping level ( $\text{Cu/Mn}_{\text{pre}} = 0.01\text{--}0.10$ ), CuO is attached on the external surface of OMS. Physisorption and oxidative destruction of HCBz are hindered due to the reduction of textural properties and the amount of surface labile oxygen (SLO). At medium ( $\text{Cu/Mn}_{\text{pre}} = 0.20$ ) and high Cu doping level ( $\text{Cu/Mn}_{\text{pre}} = 0.40\text{--}0.80$ ), CuO/Cu<sup>2+</sup> is incorporated into the framework or even enters into the tunnel structure of OMS. The textural properties and the amount of SLO are significantly promoted, resulting in the remarkable adsorption and destruction performance. Additionally, the stability of OMS is greatly enhanced by Cu doping, which can be ascribed to the rapid removal of surface chloride catalyzed by CuO.

© 2013 Elsevier B.V. All rights reserved.

## 1. Introduction

Hexachlorobenzene (HCBz) is one of the unintentionally produced persistent organic pollutants (unintentional POPs) defined by the Stockholm Convention. Its emission concentration is several orders of magnitude higher than PCDD/Fs in the flue gas of waste combustion [1,2] and industrial processes [3], but attracts less attention. The catalytic destruction of HCBz is an important pollutant control issue, not only because HCBz is a toxic organic but also it is an excellent surrogate of other unintentional POPs in the catalytic destruction reaction [4–6]. Moreover, the fully chlorinated structure of HCBz also helps us screening catalyst that is resistant to chlorine poisoning.

Octahedral molecular sieve (OMS) with cryptomelane structure (known as OMS-2) is a type of  $\text{MnO}_x$  with one-dimensional tunnel structure constituted by  $2 \times 2$  edge-shared  $\text{MnO}_6$  octahedral units and supported by tunnel  $\text{K}^+$  [7]. Recently, OMS as an environmental catalyst has shown high activities on adsorption [8,9] and oxidative destruction [8,10,11] of volatile organic compounds and CO. Previously, we also found that OMS is highly effective for the removal of low concentration gaseous HCBz [5]. To further enhance the catalytic performance, OMS can be doped by various cations, such

as  $\text{V}^{5+}$ ,  $\text{Cr}^{4+}$ ,  $\text{Fe}^{3+}$ ,  $\text{Co}^{2+}$ , and  $\text{Cu}^{2+}$  [12–15]. Among those dopants,  $\text{Cu}^{2+}$  showed the highest capacity to improve the activity of OMS on CO [15,16], dimethyl ether [15], and propanol [17] oxidation. Therefore, the doping of Cu onto OMS to enhance HCBz oxidative destruction activity appears promising.

Cu doped OMS can be prepared by impregnation [18], ball milling [16], reflux [13,19], and multi-step hydrothermal methods [20]. Different methods may lead to various fates of Cu species in the OMS structure, which could be loaded on the surface [18], incorporated into the framework [13,19], or entered into the tunnel [13]. Recent researches have reported the positive effect of Cu dopant on the redox properties of OMS [15,16,18]. Unfortunately, those results were obtained at a single Cu doping concentration and/or single Cu location. The effects of doping concentration on Cu location in OMS and the resultant impacts on textural properties, morphology, and reactivity of oxygen species have not been fully investigated. To the best of our knowledge, the adsorption/destruction activity and stability of Cu-OMS for the removal of gaseous HCBz have not been reported previously. The catalyst structure–activity correlation, surface reaction, and active site regeneration mechanism have not been proposed as well.

Consequently, this study was undertaken to advance current knowledge in activity and mechanism of HCBs removal by Cu-OMS. In this study, Cu-OMS was synthesized by one-step hydrothermal method. The Cu locations within OMS at different Cu doping levels were determined by various characterization techniques. The

\* Corresponding author. Tel.: +86 10 62787137; fax: +86 10 62794006.

E-mail address: [yg-den@mail.tsinghua.edu.cn](mailto:yg-den@mail.tsinghua.edu.cn) (G. Yu).

catalytic performance of Cu-OMS for HCBz removal was investigated in continuous and batch tests. Crucial steps, including physisorption, molecule activation, oxidative destruction, and active site regeneration were identified and found to be associated with Cu location.

## 2. Materials and methods

### 2.1. Catalyst preparation

OMS was prepared by the hydrothermal method [5,21]: 3.2 mmol  $\text{KMnO}_4$  and 1.2 mmol  $\text{MnSO}_4 \cdot \text{H}_2\text{O}$  were dissolved in 70 mL distilled water. The mixture was transferred into a Teflon-lined stainless steel autoclave (100 mL) and heated at  $160^\circ\text{C}$  for 12 h. After that, the OMS were filtered, washed and dried at  $105^\circ\text{C}$  for 30 min followed by calcination in air at  $400^\circ\text{C}$  for 4 h. Cu-OMS was prepared by adding different amount of  $\text{CuSO}_4 \cdot 5\text{H}_2\text{O}$  into the precursor solution before hydrothermal reaction. The resultant catalyst denoted as Cu(0.01)-, Cu(0.1)-, Cu(0.2)-, Cu(0.4)-, Cu(0.6)-, and Cu(0.8)-OMS with the number referring to the Cu/Mn molar ratio in the precursor solution ( $\text{Cu}/\text{Mn}_{\text{pre}}$ ) of 0.01, 0.1, 0.2, 0.4, 0.6, and 0.8, respectively.

Cu/OMS and CuO were chosen as reference catalysts. Cu/OMS was prepared via impregnation method. OMS was immersed in  $\text{Cu}(\text{NO}_3)_2$  solution with  $\text{Cu}/\text{Mn}_{\text{pre}}$  of 0.2. The slurry was ultrasonically treated for 30 min and then transferred to rotary evaporator and dried for 1 h, followed by calcination at  $400^\circ\text{C}$  for 4 h in air. Pure CuO was obtained from Sinopharm Chemical Reagent (Shanghai, China).

Before use, the catalyst powder was compressed into flakes in a hydraulic press, followed by crushing and sieving to 40–60 meshes (0.25–0.42 mm) to insure the uniform bulk density (ca.  $1 \text{ cm}^3 \text{ g}^{-1}$ ).

### 2.2. Catalyst characterization

Nitrogen physisorption, hydrogen temperature programmed reduction ( $\text{H}_2$ -TPR), oxygen temperature programmed desorption ( $\text{O}_2$ -TPD), and ammonia temperature programmed desorption ( $\text{NH}_3$ -TPD) were conducted on Quantachrome Autosorb iQ gas sorption system. Detail procedures were described as follows:

- (1) Surface area was obtained via  $\text{N}_2$  adsorption at 77 K. Pore distribution analysis was conducted by non-local density functional theory (NLDFT) model.
- (2)  $\text{H}_2$ -TPR analysis: 50 mg catalyst was heated to  $200^\circ\text{C}$  and purged with He for 1 h. After that, a mixture of 5%  $\text{H}_2/\text{Ar}$  ( $60 \text{ cm}^3 \text{ min}^{-1}$ ) was purged into the reaction tube for TPR reaction. The temperature was increased at a rate of  $10^\circ\text{C min}^{-1}$ , and the  $\text{H}_2$  consumption was monitored by TCD detector.
- (3)  $\text{NH}_3$ -TPD analysis: 100 mg catalyst was loaded and pre-treated in the same way of  $\text{H}_2$ -TPR. After that, the catalyst was purged with 10%  $\text{NH}_3/\text{He}$  at  $100^\circ\text{C}$ . Desorption of  $\text{NH}_3$  was carried out from 100 to  $450^\circ\text{C}$  at a heating rate of  $10^\circ\text{C min}^{-1}$  in He. This temperature was maintained for 1 h to ensure complete desorption.
- (4)  $\text{O}_2$ -TPD analysis: 100 mg catalyst was heated to  $110^\circ\text{C}$  and purged with He for 1 h to remove surface  $\text{H}_2\text{O}$  and physical adsorbed oxygen. Then the catalyst was purged with He and heated from 100 to  $900^\circ\text{C}$  at a rate of  $10^\circ\text{C min}^{-1}$ . The release of  $\text{O}_2$  was monitored using TCD detector.

X-ray diffraction (XRD) analysis was conducted on D/MAX-RB (Rigaku) with  $\text{Cu K}\alpha$  radiation. Raman spectra were obtained with a Renishaw RM 2000 confocal microscope excited at 633 nm using a He–Ne laser. X-ray photoelectron spectroscopy (XPS) analysis was

conducted on PHI-5300 electron spectrometer. The morphology of catalysts was observed on JSM-7401F field emission scanning electron microscope (FESEM), and the elemental composition was analyzed by energy-dispersive X-ray spectroscopy (EDS).

### 2.3. Catalytic activity test

#### 2.3.1. Continuous reaction

The configuration of the catalytic reactor has been described in our previous studies [22]. Briefly, HCBz powder was placed in the heating chamber and vaporized gradually by elevating the temperature, resulting in gas concentration of  $7.6 \pm 0.3 \text{ mg N m}^{-3}$  (ca. 0.6 ppm, the detection limit is  $50 \mu\text{g N m}^{-3}$ ). The HCBz vapor was purged into quartz reactor with  $220 \text{ mL min}^{-1}$  of carrier gas (10%  $\text{O}_2$  and 90%  $\text{N}_2$ ) and reacted with 20 mg catalyst pellets (GHSV of  $660,000 \text{ h}^{-1}$ ) at predetermined temperature. Off-gas was scrubbed in cold acetone and hexane maintained at  $0^\circ\text{C}$ . After the reaction, two adsorptive solvents were mixed, spiked with internal standard (1,2,4,5-tetrabromobenzene), and analyzed by GC–MS (Shimadzu QP2010). Residual HCBz on catalysts was extracted by ultrasonic extraction (twice by 15 mL hexane) and analyzed as well (the detection limit is  $0.1 \text{ mg g}^{-1}$ ).

For the 30 min activity test (Section 3.2.1), off-gas sampling was started from the beginning of the reaction. Fresh catalyst was used in each run and triplicates were obtained at each temperature. As for the adsorption experiment (Section 3.2.2) and stability test (Section 3.2.3), catalyst was continuously exposed to gaseous HCBz for 10–10.5 h. The 30 min off-gas sampling was conducted at the interval of 2 h to evaluate the catalytic performance. Long-term sampling lasted for the whole reaction was also performed to investigate the adsorption/destruction capacity.

The removal efficiency (RE), adsorption efficiency (AE) and destruction efficiency (DE) are defined as follows:

$$RE(\%) = \frac{(R_{in} - R_{out})}{R_{in}} \times 100\% \quad (1)$$

$$AE(\%) = \frac{R_{cat}}{R_{in}} \times 100\% \quad (2)$$

$$DE(\%) = RE(\%) - AE(\%) \quad (3)$$

where  $R_{in}$  ( $\mu\text{g}$ ) is the amount of HCBz in the inlet gas.  $R_{out}$  ( $\mu\text{g}$ ) and  $R_{cat}$  ( $\mu\text{g}$ ) are the amount of HCBz collected by gas sampler and extracted from catalyst, respectively.

#### 2.3.2. Batch reaction

The procedure of batch reaction has been described in previous studies [22]. Briefly, HCBz was spiked on catalyst to reach a loading of  $40 \text{ mg g}^{-1}$ . The mixture was sealed with air in glass ampoules. Then the ampoules were placed in the furnace (preheated to  $300^\circ\text{C}$ ) and reacted for predetermined periods (10–40 min). After the reaction, the ampoules were taken out and quenched at room temperature. In order to analyze the residual HCBz and organic intermediates, ampoules were crushed and extracted by hexane, followed by GC–MS analysis. The selectivity of intermediate was calculated as follow:

$$\text{Selectivity}(\%) = \frac{iN_i}{6N} \times 100\% \quad (4)$$

where  $N_i$  is the molar mass of intermediate with  $i$  being chlorine atoms in molecule and  $N$  the molar mass of destructed HCBz. For the analysis of chloride ( $\text{Cl}^-$ ), the ampoules were crushed and extracted by 15 mL ultra pure water, followed by ionic chromatography (IC, DIONEX ICS2000) analysis. The selectivity of  $\text{Cl}^-$  was also calculated via Eq. (4).

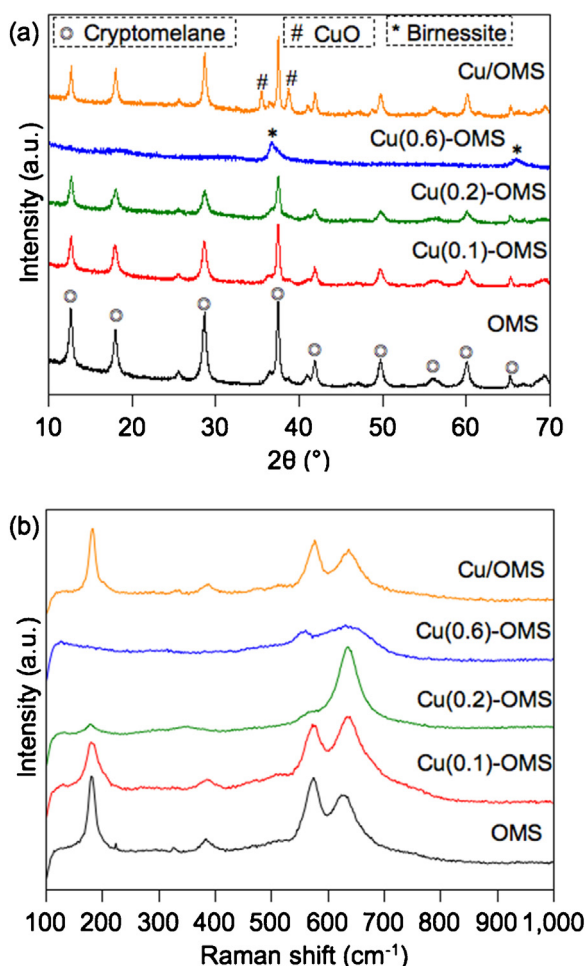


**Fig. 1.** (a) XRD patterns and (b) Raman spectra of catalysts. Cu(0.01)- and Cu(0.1)-OMS have identical XRD pattern and Raman spectra. Cu(0.4)-, Cu(0.6)-, and Cu(0.8)-OMS have identical XRD patterns and Raman spectra.

### 3. Results and discussion

#### 3.1. Catalytic characterization

##### 3.1.1. XRD, Raman spectra, morphology and elemental analysis

Fig. 1a illustrates crystalline structure of OMS, Cu-OMS, and Cu/OMS. The XRD pattern of pristine OMS corresponds to cryptomelane (PDF 29-1020) in I (4/m) space group. The diffraction peaks of all Cu-OMS catalysts become broader with the increase of Cu doping, but no additional peaks of CuO are observed. The crystallite sizes of pristine OMS, Cu(0.1)-, and Cu(0.2)-OMS calculated by Debye–Scherrer equation are 17, 16, and 12 nm, respectively. The results indicate that Cu doping interfere the crystallization of Cu-OMS. With the further increase of Cu/Mn<sub>pre</sub>, Cu(0.4)-, Cu(0.6)-, and Cu(0.8)-OMS are transformed into birnessite (PDF 80-1098) structure (birnessite type MnO<sub>2</sub>, known as octahedral layer molecular sieve [23], will be also nominated as OMS in this study for simplicity). In contrast, the crystalline of Cu/OMS is barely changed except for the diffraction peaks of CuO at 35° and 40°. Lattice vibration of catalysts was investigated by Raman spectra (Fig. 1b). Pristine OMS exhibits four distinct Raman peaks. The peaks at 181 and 386 cm<sup>-1</sup> can be ascribed to the deformation modes of Mn–O–Mn, while the peaks at 630 and 578 cm<sup>-1</sup> can be assigned to the Mn–O vibrations that are orthogonal and along the direction of the MnO<sub>6</sub> octahedral double chains [10,19]. With the increase of Cu doping level, the Mn–O bond on Cu-OMS becomes weaker, while that on Cu/OMS is not affected by Cu doping.

The morphology of catalyst was observed by FESEM. Fig. 2a illustrates one-dimensional nano-rod morphology of pristine OMS. Similar images are also observed on Cu(0.01)- and Cu(0.1)-OMS (data not shown). For Cu(0.2)-OMS, small clusters are found between nano-rod (Fig. 2b). The inserted figure points out that these clusters are constituted by nano-rod with shorter length. The intergrowth of layer along with nano-rod structures is observed on Cu(0.4)-OMS (Fig. 2c), implying the transition of morphology. The rod structure is completely disappeared and the layer structure grows larger on Cu(0.6)-OMS (Fig. 2d) and Cu(0.8)-OMS (data not shown).

Bulk elemental composition of catalysts was measured by EDS (Table 1). The bulk Cu/Mn molar ratio (Cu/Mn<sub>bulk</sub>) of Cu-OMS is lower than Cu/Mn<sub>pre</sub>, implying only part of Cu<sup>2+</sup> precursor could be doped into OMS during hydrothermal synthesis. The Cu/Mn<sub>bulk</sub> reaches stable at ca. 0.25 when Cu/Mn<sub>pre</sub> exceeds 0.4, implying that the structure of OMS has limited Cu uptake capacity. On the contrary, all of the Cu<sup>2+</sup> precursor could be loaded on Cu/OMS prepared by impregnation method. It is also observed that the K/Mn<sub>bulk</sub> of Cu-OMS decreases with the increasing Cu doping level except for that of Cu/OMS remains intact.

Surface elemental composition of catalysts was analyzed by XPS (Table 1). The comparison of EDS and XPS reveals the heterogeneity of catalyst. For Cu(0.01)- and Cu(0.1)-OMS, the Cu/Mn<sub>surf</sub> is significantly higher than Cu/Mn<sub>bulk</sub>. The diversity between surface and bulk elemental composition is subtle for Cu(0.2)-OMS and finally becomes negligible for Cu(0.4)-, Cu(0.6)-, and Cu(0.8)-OMS. Fig. S1 shows that the Mn 2p<sub>3/2</sub> peak of catalysts is at binding energy (BE) of 642.4 eV, implying the main surface manganese species are Mn (IV) [21]. For all the samples, the main Cu 2p peaks at BE (2p<sub>1/2</sub>) of 953.4 eV and BE (2p<sub>3/2</sub>) of 933.5 eV, accompanied with shake-up satellites at 940–950 eV can be observed (Fig. S1), indicating the presence of Cu(II) [24]. Thus, it can be deduced that the surface copper species of Cu-OMS and Cu/OMS are in the form of CuO.

The XRD, Raman, elemental analysis and FESEM observations reveal the locations of Cu in OMS. In the case of Cu/OMS prepared by impregnation method, all the doped CuO is found to attach on the external surface of OMS, evidenced by several experimental observations. First, the difference between surface and bulk Cu/Mn ratio indicates the surface accumulation of Cu atoms. Secondly, the intact crystalline and Mn–O vibration of Cu/OMS observed in XRD and Raman spectrum exclude the presence of framework substituted CuO. Thirdly, the K/Mn<sub>bulk</sub> of Cu/OMS is the same as that of OMS, which further rules out the possibility that Cu<sup>2+</sup> exchange with the tunnel K<sup>+</sup>.

As for Cu-OMS prepared by hydrothermal method, the fate of Cu is affected by doping level. At low Cu doping level, CuO seems to be attached on the external surface of Cu(0.01)- and Cu(0.1)-OMS (Scheme 1a), which is also supported by the surface accumulation of Cu atoms and the intact crystal structure. Since the growth of crystal is a kinetic process, the growth rate is positively correlated with precursor concentration (phenomena have been observed on the growth of ZnO [25] and CdSe [26]). The growth of OMS crystal might be faster than that of CuO at low Cu/Mn<sub>pre</sub>. As a result, the OMS nano-rod might be formed at first, followed by the growth of CuO on its external surface.

At medium doping level, CuO is incorporated into the framework of Cu(0.2)-OMS (Scheme 1b), which is directly supported by the similar values of Cu/Mn<sub>surf</sub> and Cu/Mn<sub>bulk</sub>. The broadened XRD peaks imply that the incorporation of CuO impedes the crystallization of OMS. Raman spectra further indicate that the doping of CuO distorts the Mn–O–Mn bond vibration. According to King'odu et al. [19], the MnO<sub>6</sub> units of OMS can be substituted by CuO<sub>6</sub> units, as cation Cu<sup>2+</sup> preferably stabilize as six-coordinate structure. At Cu/Mn<sub>pre</sub> of 0.20, OMS and CuO probably have comparable



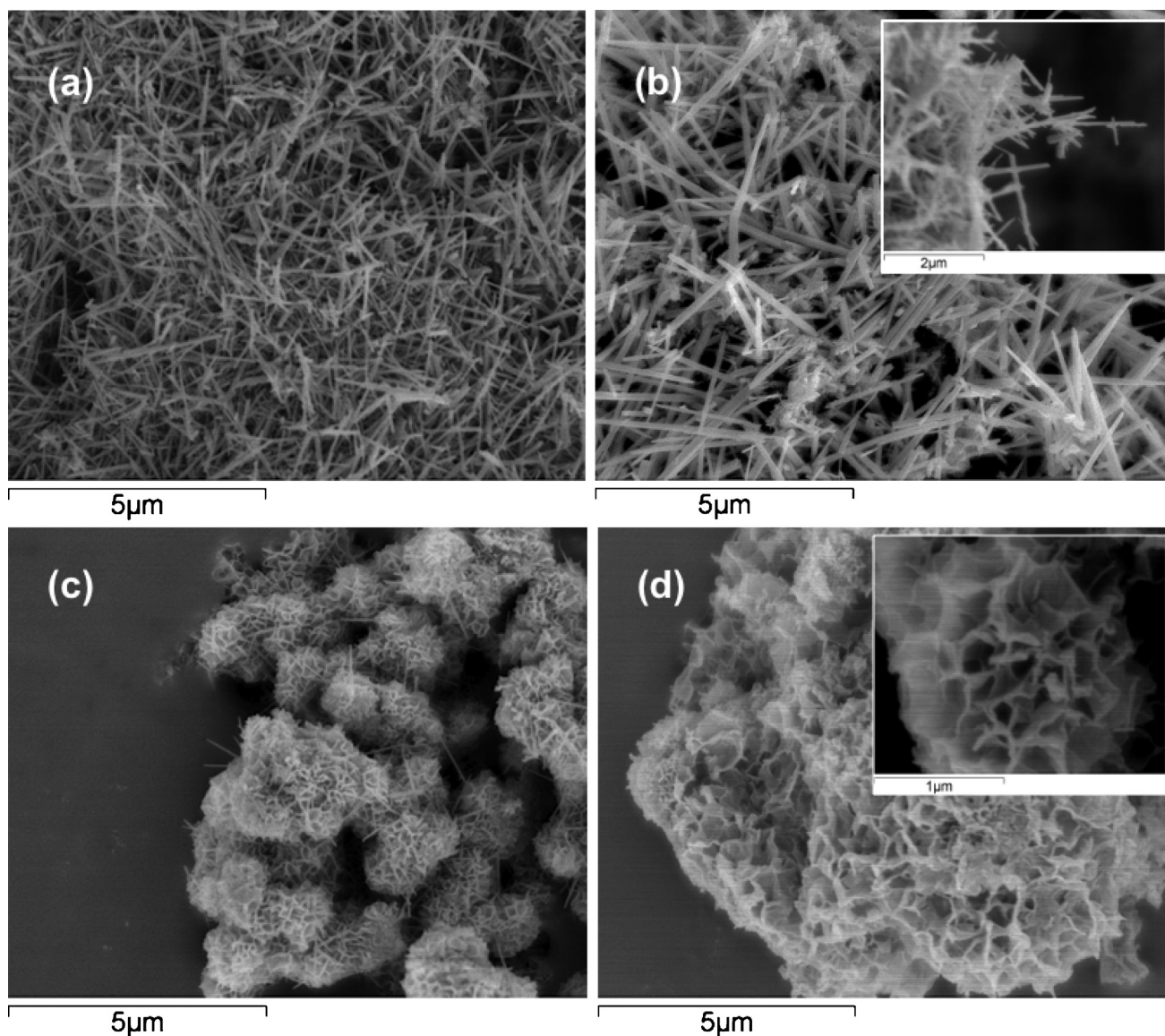


**Fig. 2.** FESEM images of (a) pristine OMS, (b) Cu(0.2)-OMS, (c) Cu(0.4)-OMS, and (d) Cu(0.6)-OMS.

crystallizing rate, hence the  $\text{CuO}_6$  units can be embedded into OMS during the self-assemble process of  $\text{MnO}_6$  units.

At high Cu doping level (i.e. Cu(0.4)-, Cu(0.6)-, and Cu(0.8)-OMS), more CuO is incorporated into the framework. Hence the crystalline structure is significantly impeded. Moreover, the excessive  $\text{Cu}^{2+}$  affects the tunnel structure of OMS (Scheme 1c). The Raman peaks

at 630 and 578  $\text{cm}^{-1}$ , which are indicators of well-developed  $2 \times 2$  tunnel structure [19], disappear in Cu(0.6)-OMS. Theoretically,  $\text{Cu}^{2+}$  with smaller ionic radius (0.73 Å) can by-pass  $\text{K}^+$  (1.38 Å), enters into the tunnel, or even expels  $\text{K}^+$  during the hydrothermal synthesize. Therefore the gradual reduction of  $\text{K}/\text{Mn}_{\text{bulk}}$  on Cu-OMS at low and medium Cu doping level is probably due to the partial

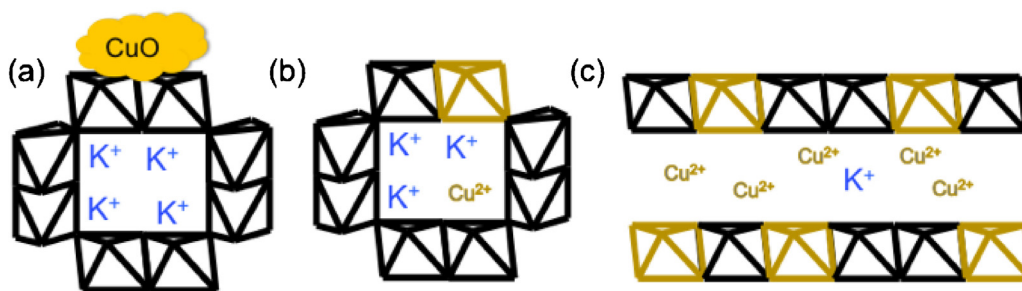
**Table 1**  
Elemental composition and textural properties of catalysts.

	Bulk composition <sup>a</sup>				Surface composition <sup>b</sup>				BET ( $\text{m}^2 \text{g}^{-1}$ )	PV <sup>c</sup> ( $\text{cm}^3 \text{g}^{-1}$ )
	% K	% Mn	% Cu	Cu/Mn <sub>bulk</sub>	% K	% Mn	% Cu	Cu/Mn <sub>surf</sub>		
OMS	12.7	87.3	–	–	16.7	83.3	–	–	61	0.29
Cu(0.01)-OMS	11.0	88.5	0.4	0.005	13.3	77.8	8.9	0.11	35	0.22
Cu(0.1)-OMS	9.0	84.0	7.1	0.08	10.9	79.1	10.0	0.13	41	0.20
Cu(0.2)-OMS	8.5	81.0	10.5	0.13	9.5	79.1	11.4	0.14	93	0.30
Cu(0.4)-OMS	1.9	77.0	21.1	0.27	1.1	78.6	20.3	0.26	204	0.82
Cu(0.6)-OMS	1.4	78.5	20.0	0.25	0.5	77.8	21.7	0.28	215	0.74
Cu(0.8)-OMS	1.7	78.6	19.7	0.25	0.5	79.2	20.3	0.26	190	0.68
Cu/OMS	10.8	74.3	14.9	0.20	17.4	61.5	21.1	0.34	22	0.14

<sup>a</sup> Bulk elemental composition was obtained by EDS analysis.

<sup>b</sup> Surface elemental composition was obtained by XPS analysis.

<sup>c</sup> Pore volume (PV) was obtained by NLDFT model.



**Scheme 1.** The Cu location within OMS synthesized at (a) low, (b) medium and (c) high Cu doping level.

exchange of pore mouth  $K^+$  by  $Cu^{2+}$ . With the further increase of Cu doping level, more  $Cu^{2+}$  enters into the tunnel. As a result, the  $2 \times 2$  tunnel is transformed into layer structure. The morphology transformation of Cu-OMS from rod to layer structure is well illustrated by FESEM (Fig. 4).

### 3.1.2. Textural, redox properties and surface acidity

The textural properties of OMS seem to be affected by Cu location. The reduction of surface area and pore volume on Cu(0.01)-, Cu(0.10)-OMS and Cu/OMS is observed (Table 1). Pore size distribution analysis (Fig. S2) further indicates the mesopores with the size of 3–10 nm are reduced on these samples. Therefore, it can be concluded that the growth of external CuO fills the mesopore of OMS, resulting in the suppressed textural properties. Interestingly, if CuO is incorporated into the framework of rod-like OMS (i.e. Cu(0.2)-OMS), the surface area is significantly increased due to the reduction of crystallite size and rod length. If  $Cu^{2+}$  further enters into the tunnel structure (i.e. Cu(0.4)-, Cu(0.6)- and Cu(0.8)-OMS), OMS achieves the largest surface area and uniform mesopore at 3.8 nm, which is probably contributed by the interspace between layer structure.

The reducibility of catalyst was evaluated by  $H_2$ -TPR (Fig. 3). The TPR profiles of catalysts are deconvoluted into three peaks, marked as  $\alpha$ ,  $\beta$ , and  $\gamma$ .  $\alpha$  peak can be assigned to the consumption of surface labile oxygen (SLO).  $\beta$  and  $\gamma$  peaks with the peak area ratio of 2:1 can be ascribed to successive reductions of  $MnO_2 \rightarrow Mn_3O_4 \rightarrow MnO$  [27]. More specifically,  $\beta$  peak is further deconvoluted into two overlapping peaks ( $\beta'$  and  $\beta''$ ), which are associated with the reduction of  $MnO_6$  octahedral in different configurations [14].  $\beta'$  peak possibly corresponds to the reduction of  $MnO_6-\square$  (" $\square$ " stands for a vacant site in  $2 \times 2$  tunnel) while  $\beta''$  peak corresponds to the reduction of  $MnO_6-K^+$ .

Generally, the peak position of Cu-OMS and Cu/OMS shifts to lower temperature compared with OMS, implying the enhanced reducibility. Cu(0.01)-, Cu(0.1)-OMS and Cu/OMS have slightly larger  $\alpha$  peak in comparison with OMS, indicating the promoted activity of SLO. As reported by Liu et al. [18],  $Cu^{2+}-O-Mn^{4+}$  entities are formed at the interface between CuO and OMS. Due to the diversity of Pauling's scale electronegativity of  $Cu^{2+}$  (1.5) and  $Mn^{4+}$  (2.0) [28], the  $O_{lat}$  in Cu–O–Mn bond is activated via electronic delocalization effect [16]. The  $\alpha$  peak becomes even larger on Cu(0.2)- and Cu(0.6)-OMS. The results suggest that more Mn–O–Cu interfaces are created when CuO is incorporated into the framework of OMS. Cu(0.6)-OMS shows only one  $\beta$  peak, implying the uniform interaction between  $MnO_6$  and tunnel cation, which is another indication that excessive  $Cu^{2+}$  replaces  $K^+$  and occupies the empty sites of tunnel. The  $\beta'$  peak of Cu/OMS is larger than  $\beta''$  peak, probably due to the simultaneous reduction of CuO cluster [29] and  $MnO_6-\square$  units.

To identify and quantify different oxygen species,  $O_2$ -TPD analysis was conducted. The  $O_2$ -TPD spectrum in Fig. 4 can be separated into three regions: low temperature (LT,  $<400^\circ C$ ), medium temperature (MT,  $400-700^\circ C$ ), and high temperature (HT,  $>700^\circ C$ ).

The LT peaks correspond to SLO desorption [5], which can be further deconvoluted into two components: peak at lower temperature is ascribed to desorption of loosely bound chemisorbed oxygen ( $O_2^-$ ,  $O_2^{2-}$ ) and the other one is assigned to the evolution surface lattice oxygen ( $O^{2-}$ , denoted as  $O_{lat}$ ). The MT peaks correspond to the evolution of sub-surface  $O_{lat}$ , and the HT peaks are assigned to the evolution of bulk  $O_{lat}$ . The amount of desorbed  $O_2$  is estimated by integrating the area of  $O_2$ -TPD curves (Table 2). Surprisingly, the improved activity of SLO (observed in  $H_2$ -TPR) does not necessarily lead to the increasing amount of SLO. In fact, Cu(0.01)-, Cu(0.1)-OMS, and Cu/OMS have lower amount of SLO in comparison with pristine OMS. It is suspected that the surface of these catalysts is partially covered by  $Cu_2O$  after the decomposition of CuO at LT in  $O_2$ -TPD analysis. Since the further decomposition of  $Cu_2O$  will not occur until  $800^\circ C$  [30], the release of  $O_{lat}$  from OMS is hindered. As for Cu(0.2)- and Cu(0.6)-OMS without external CuO,

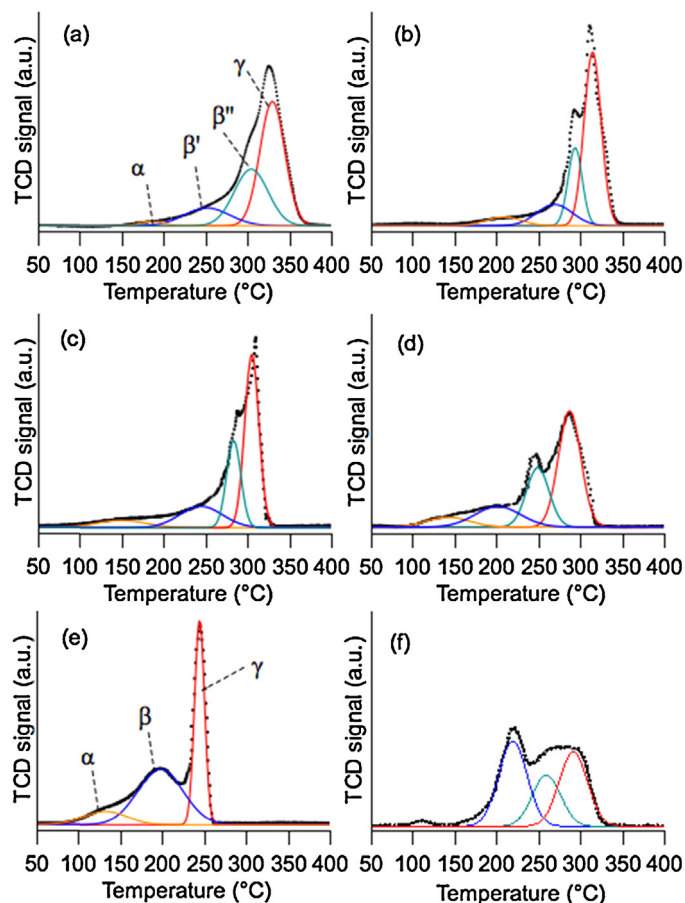


**Fig. 3.**  $H_2$ -TPR profiles of (a) pristine OMS, (b) Cu(0.01)-OMS, (c) Cu(0.1)-OMS, (d) Cu(0.2)-OMS, (e) Cu(0.6)-OMS and (f) Cu/OMS.

**Table 2**Quantitative results of O<sub>2</sub>-TPD and acidity analysis, and TOF calculation.

	SLO ( $\mu\text{mol g}^{-1}$ )	Total oxygen evolution ( $\mu\text{mol g}^{-1}$ )	Acidity ( $\mu\text{mol g}^{-1}$ )	TOF <sub>SLO</sub> ( $\text{s}^{-1}$ )	TOF <sub>Mn</sub> ( $\times 10^{-3} \text{s}^{-1}$ )
OMS	175	438	661	0.06	0.9
Cu(0.01)-OMS	62	461	586	0.32	1.6
Cu(0.1)-OMS	85	478	859	0.52	3.9
Cu(0.2)-OMS	207	680	1120	0.33/0.36 <sup>a</sup>	6.3/4.5 <sup>a</sup>
Cu(0.4)-OMS	472	890	2382	–	–
Cu(0.6)-OMS	498	871	2331	0.10	4.0
Cu/OMS	125	868	794	–	–

<sup>a</sup> TOF<sub>SLO</sub> of 0.36 s<sup>−1</sup> and TOF<sub>Mn</sub> of 4.5 × 10<sup>−3</sup> s<sup>−1</sup> were calculated according to stability test operated at 880,000 h<sup>−1</sup>.

the amount of SLO is positively correlated with the doping level (Table 2). Moreover, the largest fraction of chemisorb oxygen is observed in Cu(0.6)-OMS, which can be explained as the increase of surface defect creates more sites for the dissociative adsorption of oxygen molecule [31].

We also found that the doping of Cu will accelerate bulk thermal decomposition as more O<sub>lat</sub> is released at MT, indicating the enhanced mobility of bulk O<sub>lat</sub>. This result probably due to the formation of synergetic oxygen vacancies of Cu–□–Mn [32] during O<sub>2</sub>-TPD treatment, which facilitate the transportation of O<sub>lat</sub> from bulk to surface.

Surface acidity of catalysts was investigated by NH<sub>3</sub>-TPD. The TPD profiles (Fig. S3) of OMS, Cu-OMS, and Cu/OMS show that most of the NH<sub>3</sub> is desorbed before 400 °C, implying the presence of weak and moderate acid sites. The quantification results of the desorbed NH<sub>3</sub> shown in Table 2 indicate that the doping of Cu, regardless of the preparation route, promotes NH<sub>3</sub> adsorption on OMS. NH<sub>3</sub> can be adsorbed on Lewis sites (Mn<sup>n+</sup>) [14,33] and Brønsted sites

(Mn–O–H) [34] of OMS. The doping of Cu probably provides additional Lewis sites [35], resulting in the increase of surface acidity.

As mentioned in Section 3.1.1, Cu(0.4)-, Cu(0.6)- and Cu(0.8)-OMS have identical elemental composition and textural properties. They also share similar layer structure except Cu(0.4)-OMS has nano-rod impurity. In order to evaluate the effect of rod impurity on physicochemical properties, O<sub>2</sub>-TPD analysis was conducted on Cu(0.4)-OMS. As shown in Fig. S4, Cu(0.4)-OMS has sharp desorption peak of chemisorb oxygen at 150 °C, which is similar with Cu(0.6)-OMS, while the O<sub>lat</sub> desorption peak at 250 °C is less distinct, which is similar with the characters of Cu(0.1)-, Cu(0.2)-OMS and Cu/OMS. The Cu(0.4)-OMS has a hybrid O<sub>2</sub>-TPD characters of layer and rod-like Cu-OMS, which is in agreement with the intergrowth structures. Despite of the different O<sub>lat</sub> desorption pattern, the amount of SLO of Cu(0.4)-OMS is close to that of Cu(0.6)-OMS (Table 2). The comparison of NH<sub>3</sub>-TPD profiles between Cu(0.4)- and Cu(0.6)-OMS (Fig. S4 and Table 2) further confirms that these samples have similar surface acidity. Thus it is believed that the physicochemical properties of layer Cu-OMS are barely changed with Cu doping level when Cu/Mn<sub>pre</sub> exceeds 0.4.

### 3.2. Catalytic activity

#### 3.2.1. Activity test

Pristine OMS and Cu doped OMS were applied for the catalytic removal of gaseous HCBz. The inlet concentration of HCBz was set as 7.6 mg N m<sup>−3</sup> (ca. 0.6 ppm) to approach the real condition in flue gas [1,2]. High GHSV (660,000 h<sup>−1</sup>) was adopted to test catalyst activity under extreme conditions. As illustrated in Fig. 5a, the general decreasing trend of catalytic performance is: Cu(0.6)-OMS > Cu(0.2)-OMS > OMS > Cu(0.1)-OMS > Cu(0.01)-OMS > Cu/OMS, with CuO inactive for the removal of HCBz. Fig. 5b indicates that the RE of HCBz observed at 180 and 200 °C is contributed by both destruction and adsorption. The increase of temperature results in the decrease of AE and the increase of DE. Cu(0.4)-OMS has identical catalytic performance with Cu(0.6)-OMS (Fig. S4), which is in line with their similar physicochemical properties. The results confirm that it is reasonable to use Cu(0.6)-OMS as representative of layer OMS.

In general, we found that Cu(0.2)- and Cu(0.6)-OMS have high AE at low temperature and excellent DE at elevated temperature, leading to the high RE at a wide temperature range. Such “buffer capacity” might be critical for practical application. As indicated by previous studies, when combustion system is operated during the start-up or end-up stage, the flue gas is at lower temperature but contains more POPs compared with the normal combustion conditions [36,37]. With the advantage of adsorbent-catalyst dual function, Cu-OMS is suspected to store gaseous unintentional POPs at low temperature while effectively destruction them at elevated temperature. Therefore, adsorption and destruction of HCBz were investigated separately in the following section.

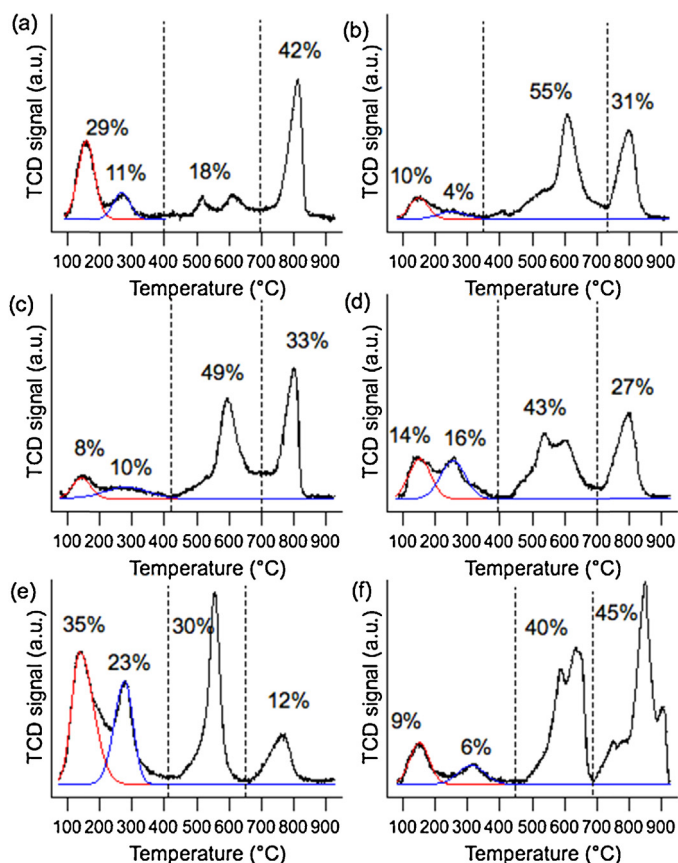


**Fig. 4.** O<sub>2</sub>-TPD profiles of (a) pristine OMS, (b) Cu(0.01)-OMS, (c) Cu(0.1)-OMS, (d) Cu(0.2)-OMS, (e) Cu(0.6)-OMS and (f) Cu/OMS.



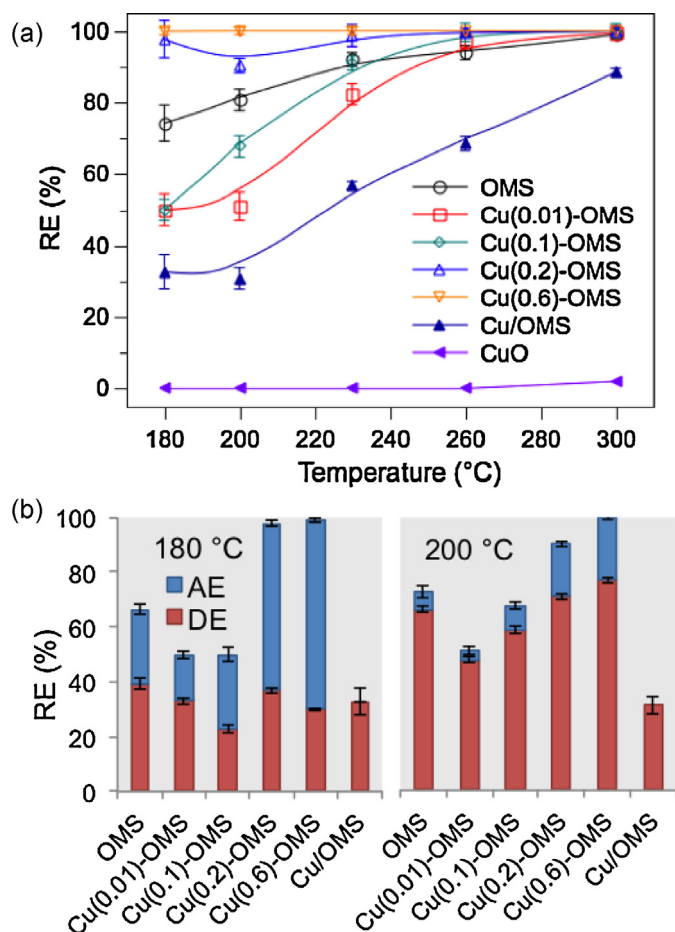


Fig. 5. (a) Removal efficiency and (b) adsorption/destruction efficiency of HCBz on fresh catalysts.

### 3.2.2. Adsorption of HCBz in $N_2$ flow

Catalysts were exposed to HCBz vapor in  $N_2$  flow for 10 h to achieve the adsorption equilibrium at 180 °C (which is the normal stack gas temperature of waste incineration process). It can be observed that the HCBz adsorption capacity decreases in the order of Cu(0.6)-OMS > Cu(0.2)-OMS > OMS > Cu(0.1)-OMS > Cu(0.01)-OMS > Cu/OMS (Fig. 6a). This tendency is consistent with the trend of changes in AE observed in Fig. 5b.

Previous studies have indicated that surface acid sites of OMS are crucial for the adsorption of small molecules, such as alcohol [38], benzene [9], and  $NH_3$  [14]. However, the poor correlation between surface acidity and adsorption capacity indicates that the adsorption of HCBz on Cu-OMS is not controlled by the interaction between molecule and surface acid sites. Considering the fact that HCBz has high boiling point (322 °C), the adsorption of HCBz on Cu-OMS might be mainly dominated by physical process. As illustrated in Fig. 6b, the HCBz adsorption capacity is determined by surface area. The correlation between adsorption capacity and pore (3.3–6.4 nm) volume (inserted figure) further indicates that the adsorption is probably due to capillary condensation mechanism. Therefore, Cu(0.6)-OMS with uniform mesopore at 3.8 nm and highest surface area shows the highest adsorption capacity.

Additionally, the destruction of HCBz under inert atmosphere is observed on OMS and Cu-OMS. The results are in agreement with previous research that the oxidation of HCBz on OMS follows the Mars-van-Krevelen mechanism [5]: HCBz was oxidized by the SLO of catalyst at first. The consumption of SLO creates surface oxygen

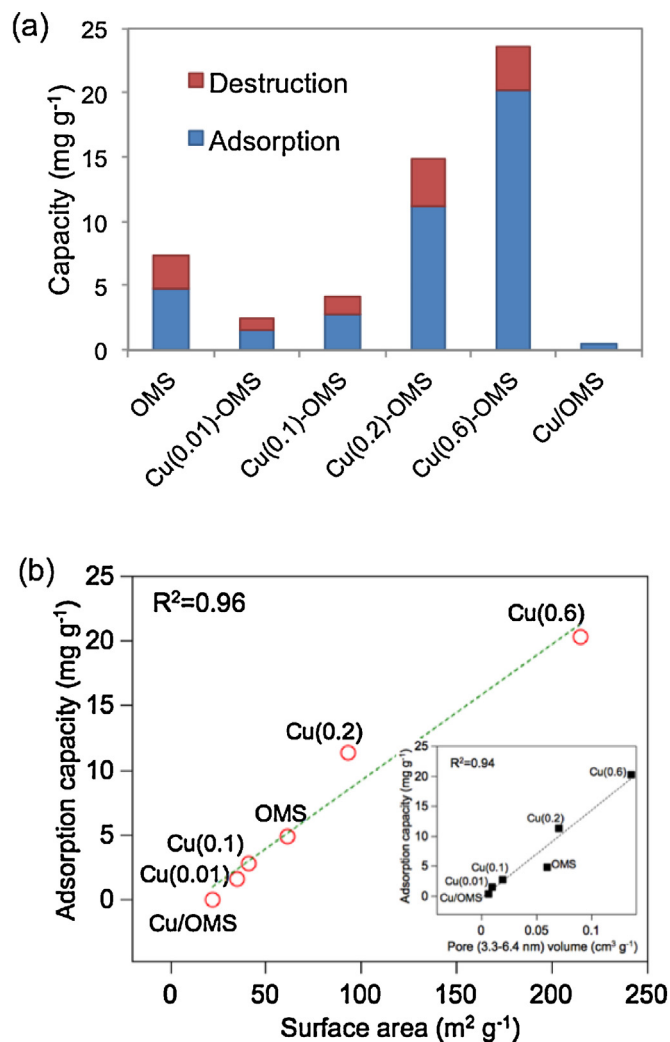


Fig. 6. Adsorption and destruction capacity measured in  $N_2$  flow.

vacancies, which is subsequently replenished by dissociative gas phase oxygen.

### 3.2.3. Batch reaction

To investigate the destruction reaction, batch reaction was conducted. In these experiments, the adsorption process was excluded, as HCBz was pre-spiked on catalysts. It is observed that the residual HCBz on catalysts decreases gradually with time (Fig. 7a). Cu(0.6)-OMS has the highest activity, followed by Cu(0.2)-OMS, OMS, Cu/OMS, and Cu(0.1)-OMS. CuO has the lowest activity in batch reaction. The results of batch reaction can be well described by first order kinetic model (Fig. S5). The rate constant  $k$  (min<sup>-1</sup>) decreases in the order of Cu(0.6)-OMS (0.17) > Cu(0.2)-OMS (0.036) > OMS (0.031) > Cu(0.1)-OMS  $\approx$  Cu/OMS (0.015 min<sup>-1</sup>), which is also linearly related with the amount of SLO (Fig. 7b). Therefore, SLO is identified as the active sites for HCBz oxidation.

The batch reaction also provides valuable information of surface reaction mechanisms, as intermediates can be retained in the sealed system after rapid quench of the reaction. Fig. 7c shows the chlorine-based selectivity of intermediates detected during the HCBz catalytic reaction (quantitative results are listed in Tables S1–S4). The activation of chlorinated organics is the crucial step prior to the oxidation [39,40]. The cleavage of C–Cl bond is the initial step of HCBz activation on OMS and Cu-OMS, which is supported by the detection of PeCBz as the major intermediate. Since HCBz has full-chlorinated structure, the transformation from HCBz

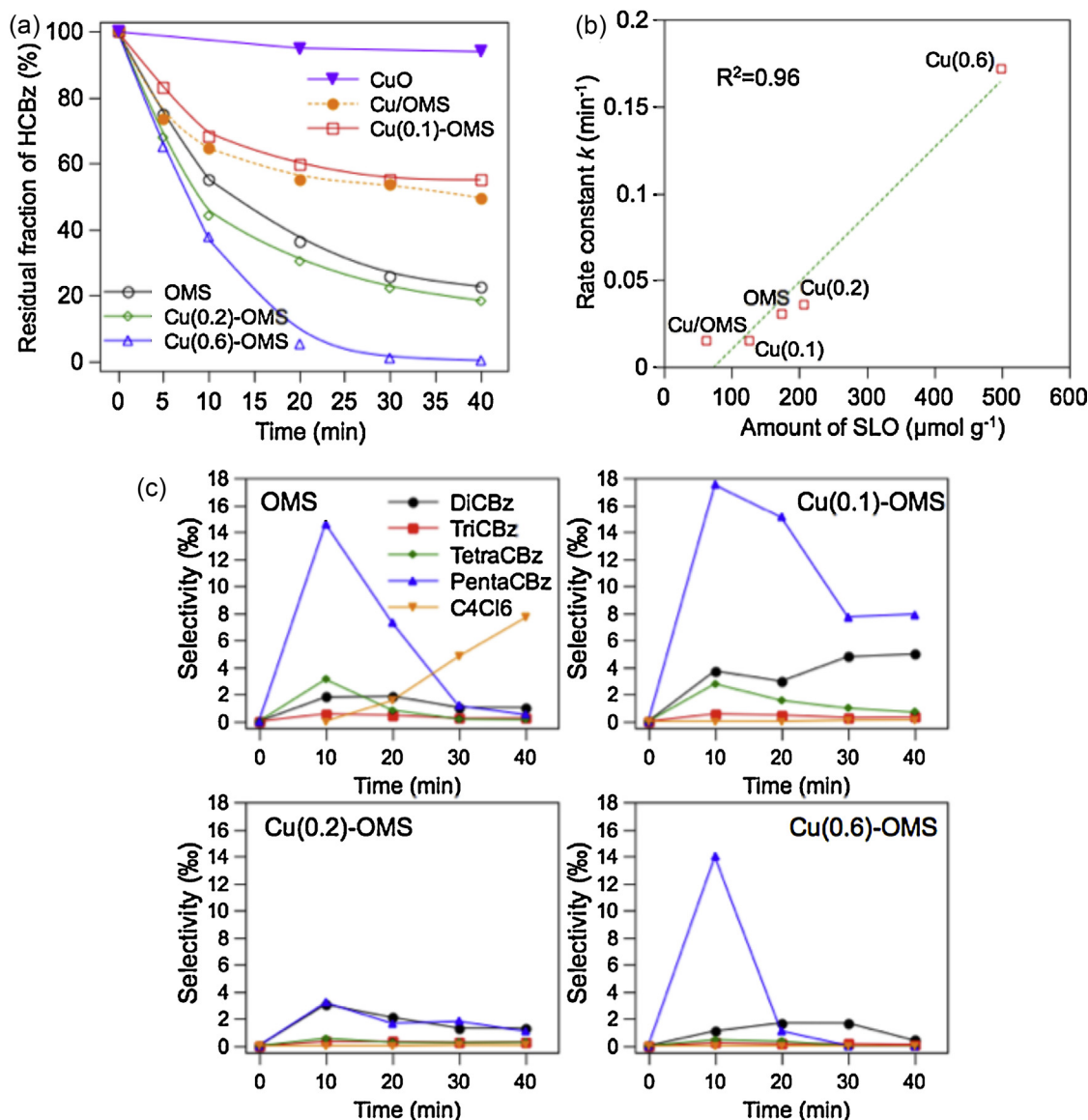


Fig. 7. (a) Residual HCBz in batch reaction, (b) SLO- $k$  correlation and (c) selectivity of organic intermediates.

to PeCBz needs extra proton. Therefore, it can be deduced that the Brønsted sites on OMS and Cu-OMS serve as the proton donor. These Brønsted sites are suspected to be the hydroxyl groups. It is reported that the surface of OMS contains large amount of  $\text{Mn}^{3+}$  and  $\text{Mn}^{2+}$  [11,41], on which hydroxyl groups will be formed due to the charge-balance (if  $\text{Mn}^{4+}$  in  $\text{MnO}_6$  unit is replaced by  $\text{Mn}^{3+}$ , hydroxyl may be formed to neutralize net charge. This process can be described as  $\text{Mn}^{4+}-\text{O}^{2-} \rightarrow \text{Mn}^{3+}-\text{OH}^-$  (or  $\text{Mn}^{2+}-(\text{OH}^-)_2$  [19]).

According to the intermediate analysis, PeCBz can be further protonated to lower chlorinated benzenes. It is observed that *para*-substituted chlorobenzenes are the major intermediates (Tables S1–S4). The main activation pathway is identified as:  $\text{HCBz} \rightarrow \text{PeCBz} \rightarrow 1,2,4,5\text{-T}_4\text{CBz} \rightarrow 1,2,4\text{-T}_3\text{CBz} \rightarrow 1,4\text{-D}_2\text{CBz}$  (Fig. 8). Since HCBz cannot enter into the tunnel of OMS due to the steric hindrance, it is suspected that the benzene ring of HCBz is attached in parallel with the external surface of OMS (Fig. 8). In this way, C–Cl bonds of HCBz can be activated simultaneously with the aid of multiple Brønsted sites.

Aside from the dechlorinated intermediates,  $\text{C}_4\text{Cl}_6$  is detected (Fig. 7c), which reveals the pathway of oxidative ring opening

reaction (Fig. 8).  $\text{C}_4\text{Cl}_4$  radical could be formed by the nucleophilic attack of SLO on benzene ring. The radical possibly complexes with Mn sites via  $\sigma$ -metal–carbon bonds, forming chlorinated metal-lacyclopentadiene intermediate [42]. Finally,  $\text{C}_4\text{Cl}_6$  is formed by ligand-transfer oxidation reaction with  $\text{MnCl}_x$  [43]. The doping of Cu on OMS does not alter the activation pathway of HCBz. However,  $\text{C}_4\text{Cl}_6$  is not detected in the reaction catalyzed by Cu-OMS. As will be discussed latter, the presence of CuO accelerate the removal of Cl from Mn atoms. Thus, it is suspected that  $\text{C}_4\text{Cl}_4$  radicals have less chance to react with  $\text{MnCl}_x$  and is rapidly oxidized by SLO on Cu-OMS.

It is also reported that CuO is active for the catalytic formation of PCDD/Fs from chlorinated precursors [44,45]. However, in this study PCDD/F were not detected by GC–MS (operated in both SCAN and SIM modes) in the batch reaction catalyzed by Cu-OMS. The results can be ascribed to two reasons: (1) oxidative destruction of HCBz is the dominant reaction on Cu-OMS. Fan et al. [46] also proved that using Cu as dopant of catalyst did not necessarily facilitate the formation of PCDD/Fs. (2) The reaction temperature (300 °C) is lower than the optimum temperature (350–500 °C) of



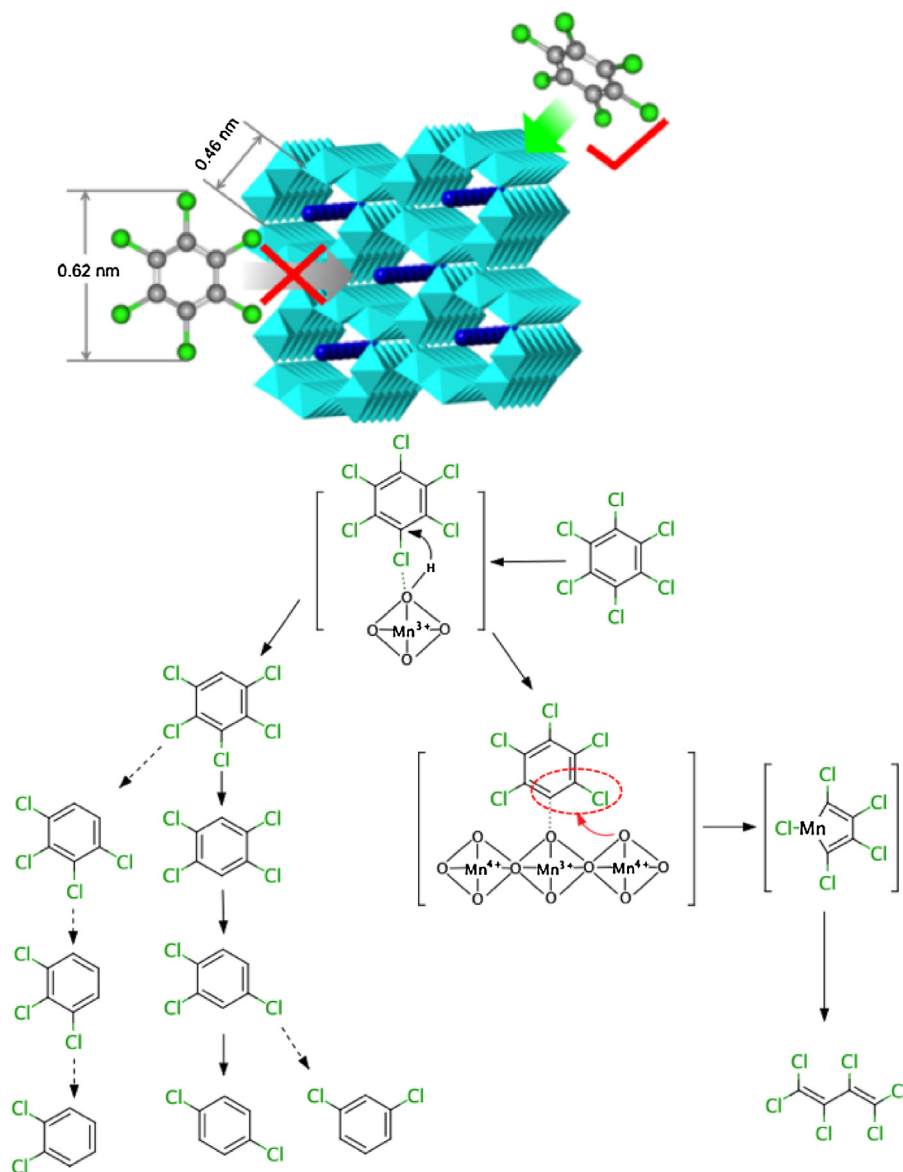


Fig. 8. Proposed mechanism of HCBz activation and oxidative ring rupture on OMS.

PCDD/F formation [45]. Using GC–HRMS (high resolution MS) to evaluate the formation potential of trace concentration PCDD/Fs on Cu–OMS is currently underway.

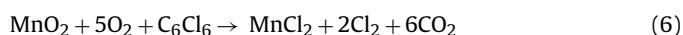
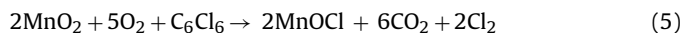
### 3.3. Stability test and active sites self-regeneration mechanism

The stability of catalysts was investigated by operating the reaction at 300 °C for 10.5 h (Fig. 9a). It is observed that the doping of Cu significantly promotes the stability of OMS. Cu(0.2)–OMS has the highest stability. Satisfactory stability of Cu(0.2)–OMS can still be observed at higher GHSV (880,000 h<sup>−1</sup>), with only 5% drop in activity after 5 h reaction. Cu(0.6)–OMS shows inferior stability than Cu(0.2)–OMS, probably due to the collapse of layer structure as the surface area reduces from 215 to 144 m<sup>2</sup> g<sup>−1</sup> after stability test.

To appropriately characterize catalyst stability, one must distinguish the true stability (active site can be rapidly self-regenerated) from the false appearance (the active site is irreversibly deactivated, but the huge number of which delays the drop of catalytic activity). The enhanced stability of Cu–OMS is unlikely due to the latter reason, as Cu(0.01)– and Cu(0.1)–OMS have less amount of SLO

but exhibit better stability compared with pristine OMS. Therefore, the enhanced stability of Cu–OMS should be ascribed to the fast regeneration of active sites.

To substantiate this speculation, the deactivation mechanism of OMS is investigated at first. As mentioned above, the destruction of HCBz involves the consumption and replenishment of SLO, which can also be interpreted as reduction and re-oxidation of surface Mn<sup>4+</sup>. For the oxidation of halogen ligand-free compound such as toluene, ethanol, and CO, the re-oxidation of surface Mn<sup>4+</sup> is fast [9,21,27]. However, this step might be impeded for the oxidation of HCBz with fully chlorinated structure. The XPS characterization indicates that the BE of Mn 2p<sub>3/2</sub> peaks of spent OMS shifts from 642.4 to 641.5 eV (Fig. 10a), which can be assigned to the formation of Mn(III) [47]. Additional shoulder peak at 640.6 eV is found, implying the presence of Mn(II) [47]. These lower valence Mn species are suspected to be oxy-chlorinated Mn(III) and deeply chlorinated Mn(II) formed by following reactions:



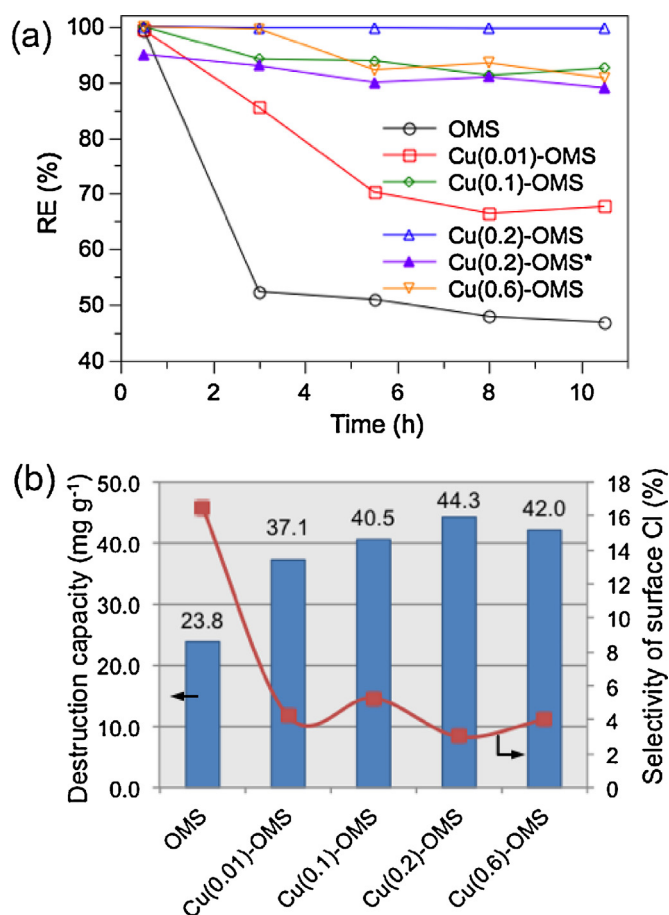
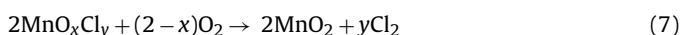


Fig. 9. (a) Stability test, (b) total destruction capacity and selectivity of surface Cl after long-term reaction (test of Cu(0.2)-OMS\* was operated at 880,000 h<sup>-1</sup>, catalyst amount is 15 mg).

The re-oxidation of chlorinated Mn is conducted via Deacon reaction [48]:



which is an endothermic reaction requiring high temperature (560 °C) [48], hence it becomes the rate-limiting step of HCBz destruction reaction, resulting in the deactivation of OMS.

In contrast, surface Mn<sup>4+</sup> on spent Cu(0.2)-OMS remains intact (Fig. 10b) while surface Cu<sup>2+</sup> is transformed to multiple states species (Fig. 10c). Two peaks at 932.4 and 934.2 eV can be assigned to the Cu 2p<sub>3/2</sub> peaks of CuCl and CuCl<sub>2</sub> [47], respectively. These results suggest that the re-oxidation of Mn<sup>4+</sup> on Cu-OMS is not inhibited, because surface chloride is prone to complex with CuO sites. Surface chloride is probably removed via the re-oxidation of CuCl<sub>x</sub>:



Reaction (8) ( $\Delta H = 7.5 \text{ kcal mol}^{-1}$ ) is more thermodynamically favorable than reaction (7) ( $\Delta H = 17.7 \text{ kcal mol}^{-1}$ ) [48]. Experimental measurement also proved that the rate of reaction (8) is 20 times higher than that of reaction (7) [49].

In order to prove the rapid removal of surface chloride on Cu-OMS, the deposition of surface chloride was evaluated. Cumulative sampling lasted for 10.5 h was conducted to quantify the total amount of destructed HCBz (normalized to per gram basis and shown in Fig. 9b). Meanwhile, surface Cl on spent catalysts was extracted by ultra pure water, and quantified by IC. Combined with

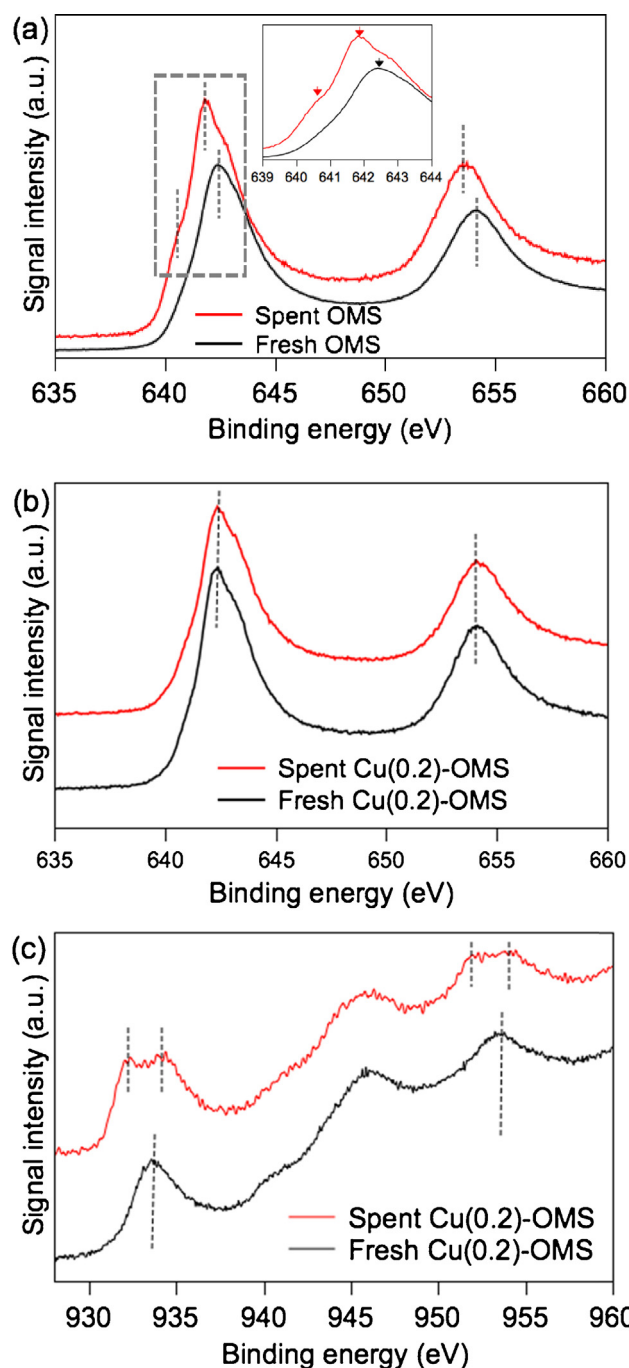


Fig. 10. Mn2p XPS peaks of (a) OMS and (b) Cu(0.2)-OMS before and after stability test. (c) Cu2p XPS peak of Cu(0.2)-OMS before and after stability test.

these results, the selectivity of surface Cl can be determined (right axial in Fig. 9b). It is found that 17% of chlorine atoms originated from destructed HCBz is deposited onto OMS. However, the deposition of surface chloride is insignificant (3–5%) on Cu-OMS. The rapid removal of surface chloride may also explain the low Cl balance in batch reaction catalyzed by Cu-OMS. As shown in Tables S1–S4, 54, 67, and 74% of the chlorine atoms from destructed HCBz is recovered as Cl<sup>-</sup> (probably originated from MnCl<sub>x</sub> or HCl) on Cu(0.1)-, Cu(0.2)-, and Cu(0.6)-OMS, which is lower than the value (92%) of OMS. It is suspected that part of the end products might be in the form of Cl<sub>2</sub>, which is released after the crush of ampule. Recently,

Dai et al. [50,51] reported that doping noble metal ( $\text{RuO}_2$ ) could accelerate the removal of surface Cl on  $\text{CeO}_2$  during the catalytic oxidation of chlorobenzene. Our finding on Cu-OMS indicates that this design strategy can also be achieved by doping inexpensive transitional metal oxide.

The activity of OMS and Cu-OMS reaches stable after 5 h reaction, which also means the consumption and regeneration of active sites are in a steady state. Therefore, the turnover frequency (TOF) of active sites can be calculated utilizing the first-order dependence on HCBz, according to the following equation:

$$\text{TOF} = - \left( \frac{Q}{\eta} \right) \times C_{\text{HCBz}} \times \ln(1 - x) \quad (9)$$

where  $Q$  is the volumetric flow ( $\text{N m}^3/\text{s}$ ),  $C_{\text{HCBz}}$  is the inlet concentration of HCBz ( $\mu\text{mol}/\text{N m}^3$ ),  $x$  is the RE at 10.5 h,  $\eta$  is the amount of active sites ( $\mu\text{mol}$ ).  $\text{TOF}_{\text{SLO}}$  and  $\text{TOF}_{\text{Mn}}$  were calculated, which is based on the amount of SLO and Mn in the reactor, respectively (Table 2). Cu-OMS shows higher TOF than OMS, which is in agreement with the enhanced reducibility evaluated by  $\text{H}_2$ -TPR. However, the actual catalytic destruction performance in flow test (Fig. 5a) is more likely to be determined by the amount of SLO, in other word “the number of active sites”. This is reasonable as the total amount of HCBz in one activity test only corresponds to 0.03–0.3% of a monolayer of the catalyst surface. The increasing amount of SLO raises the contact probability between HCBz and active sites, leads to higher performance. The framework substituted CuO will significantly increase the amount of SLO, thus Cu(0.2)- and Cu(0.6)-OMS have higher performance than other Cu-OMS and pristine OMS.

#### 4. Conclusions

Cu-OMS with different Cu location was synthesized by one-step hydrothermal method and tested for the catalytic removal of low concentration gaseous HCBz. Conclusions are drawn as follows:

- (1) CuO is attached on the external surface of Cu(0.01)- and Cu(0.1)-OMS, and incorporated into the framework of Cu(0.2)-OMS. In the presence of excessive  $\text{Cu}^{2+}$ , Cu(0.4)-, Cu(0.6)-, and Cu(0.8)-OMS are transformed into layer structure. Surface area and the amount of SLO are reduced by external CuO, but increased by framework substituted CuO. The reducibility of Cu-OMS is promoted due to the formation of Cu–O–Mn interface.
- (2) The HCBz adsorption capacity of Cu-OMS is positively correlated with surface area and pore volume. The TOF of HCBz oxidation on Cu-OMS is inline with catalyst reducibility, but the actual performance is determined by the amount of SLO. The destruction mechanism involves the molecular activation on Mn–O–H sites and the nucleophilic attack on benzene ring by SLO.
- (3) Chloride will complex with Mn–O sites after HCBz destruction, resulting in the deactivation of pristine OMS. However, Cu-OMS can achieve better stability due to the accelerated removal of surface Cl via Deacon reaction catalyzed by CuO.

#### Acknowledgments

This study was supported by the “National High Technology Research and Development Program of China (2013AA06A305)”, “Program for Changjiang Scholars and Innovative Research Team in University”, and “The Collaborative Innovation Center for Regional Environmental Quality”.

#### Appendix A. Supplementary data

Supplementary data associated with this article can be found, in the online version, at <http://dx.doi.org/10.1016/j.apcatb.2013.11.041>.

#### References

- [1] E. Wikström, M. Tysklind, S. Marklund, *Environ. Sci. Technol.* 33 (1999) 4263–4269.
- [2] M. Watanabe, Y. Noma, J. Environ. Sci. Health. A: Tox. Hazard. Subst. Environ. Eng. 45 (2010) 846–854.
- [3] B. Tian, J. Huang, B. Wang, S. Deng, G. Yu, *Chemosphere* 89 (2012) 409–415.
- [4] J.E. Lee, J. Jurng, *Catal. Lett.* 120 (2008) 294–298.
- [5] Y. Yang, J. Huang, S. Wang, S. Deng, B. Wang, G. Yu, *Appl. Catal. B: Environ.* 142–143 (2013) 568–578.
- [6] R. Weber, T. Sakurai, H. Hagenmaier, *Appl. Catal. B: Environ.* 20 (1999) 249–256.
- [7] R.N. Deguzman, Y.F. Shen, E.J. Neth, S.L. Suib, C.L. Oyoung, S. Levine, J.M. Newsam, *Chem. Mater.* 6 (1994) 815–821.
- [8] H.C. Genuino, S. Dharmarathna, E.C. Njagi, M.C. Mei, S.L. Suib, *J. Phys. Chem. C* 116 (2012) 12066–12078.
- [9] J. Luo, Q. Zhang, J. Garcia-Martinez, S.L. Suib, *J. Am. Chem. Soc.* 130 (2008) 3198–3207.
- [10] R.H. Wang, J.H. Li, *Environ. Sci. Technol.* 44 (2010) 4282–4287.
- [11] F. Wang, H. Dai, J. Deng, G. Bai, K. Ji, Y. Liu, *Environ. Sci. Technol.* 46 (2012) 4034–4041.
- [12] E. Nicolas-Tolentino, Z.-R. Tian, H. Zhou, G. Xia, S.L. Suib, *Chem. Mater.* 11 (1999) 1733–1741.
- [13] X. Chen, Y.-F. Shen, S.L. Suib, C.L. O'Young, *Chem. Mater.* 14 (2002) 940–948.
- [14] L.A. Sun, Q.Q. Cao, B.Q. Hu, J.H. Li, J.M. Hao, G.H. Jing, X.F. Tang, *Appl. Catal. A: Gen.* 393 (2011) 323–330.
- [15] M. Sun, L. Yu, F. Ye, G. Diao, Q. Yu, Z. Hao, Y. Zheng, L. Yuan, *Chem. Eng. J.* 220 (2013) 320–327.
- [16] W.Y. Hernández, M.A. Centeno, S. Ivanova, P. Eloy, E.M. Gaigneaux, J.A. Odriozola, *Appl. Catal. B: Environ.* 123–124 (2012) 27–35.
- [17] X. Chen, Y.-F. Shen, S.L. Suib, C.L. O'Young, *J. Catal.* 197 (2001) 292–302.
- [18] X.-S. Liu, Z.-N. Jin, J.-Q. Lu, X.-X. Wang, M.-F. Luo, *Chem. Eng. J.* 162 (2010) 151–157.
- [19] C.K. King'andu, N. Opembe, C.-H. Chen, K. Ngala, H. Huang, A. Iyer, H.F. Garcés, S.L. Suib, *Adv. Funct. Mater.* 21 (2011) 312–323.
- [20] R. Jothiramaniam, B. Viswanathan, T.K. Varadarajan, *Mater. Chem. Phys.* 100 (2006) 257–261.
- [21] S.H. Liang, F.T.G. Bulgan, R.L. Zong, Y.F. Zhu, *J. Phys. Chem. C* 112 (2008) 5307–5315.
- [22] Y. Yang, G. Yu, S. Deng, S. Wang, Z. Xu, J. Huang, B. Wang, *Chem. Eng. J.* 192 (2012) 284–291.
- [23] S.L. Suib, *Acc. Chem. Res.* 41 (2008) 479–487.
- [24] C.C. Chusuei, M.A. Brookshier, D.W. Goodman, *Langmuir* 15 (1999) 2806–2808.
- [25] M. Guo, P. Diao, S. Cai, J. Solid State Chem. 178 (2005) 1864–1873.
- [26] J.S. Owen, E.M. Chan, H. Liu, A.P. Alivisatos, *J. Am. Chem. Soc.* 132 (2010) 18206–18213.
- [27] V.P. Santos, M.F.R. Pereira, J.J.M. Orfao, J.L. Figueiredo, *Appl. Catal. B: Environ.* 99 (2010) 353–363.
- [28] Y. Zhang, *Inorg. Chem.* 21 (1982) 3886–3889.
- [29] J. Rodriguez, J. Kim, J. Hanson, M. Pérez, A. Frenkel, *Catal. Lett.* 85 (2003) 247–254.
- [30] P. Kirsch, J. Ekerdt, *J. Appl. Phys.* 90 (2001) 4256–4264.
- [31] V.V. Pushkarev, V.I. Kovalchuk, J.L. d'Itri, *J. Phys. Chem. C* (2004) 5341–5348.
- [32] D. Li, Q. Yu, S.-S. Li, H.-Q. Wan, L.-J. Liu, L. Qi, B. Liu, F. Gao, L. Dong, Y. Chen, *Chem. Eur. J.* 17 (2011) 5668–5679.
- [33] A.R. Gandhe, J.S. Rebello, J.L. Figueiredo, J.B. Fernandes, *Appl. Catal. B: Environ.* 72 (2007) 129–135.
- [34] Z.-M. Wang, S. Tezuka, H. Kanoh, *Chem. Lett.* 29 (2000) 560–561.
- [35] H. Sjövall, R.J. Blint, L. Olsson, *J. Phys. Chem. C* 113 (2009) 1393–1405.
- [36] H.H. Linchi Wang, J. Chang, X. Yang, G.C. Chien, W. Lee, *Chemosphere* 67 (2007) 1346–1353.
- [37] H. Tejima, M. Nishigaki, Y. Fujita, A. Matsumoto, N. Takeda, M. Takaoka, *Chemosphere* 66 (2007) 1123–1130.
- [38] J. Li, R. Wang, J. Hao, *J. Phys. Chem. C* 114 (2010) 10544–10550.
- [39] B. de Rivas, R. López-Fonseca, J.R. González-Velasco, J.I. Gutiérrez-Ortiz, *J. Mol. Catal. A: Chem.* 278 (2007) 181–188.
- [40] J.I. Gutiérrez-Ortiz, B. de Rivas, R. López-Fonseca, J.R. González-Velasco, *Appl. Catal. A: Gen.* 269 (2004) 147–155.
- [41] S.L. Suib, *J. Mater. Chem.* 18 (2008) 1623–1631.
- [42] K.P.C. Vollhardt, *Acc. Chem. Res.* 10 (1977) 1–8.
- [43] K.D. Donnelly, W.E. Fristad, B.J. Gellerman, J.R. Peterson, B.J. Selle, *Tetrahedron Lett.* 25 (1984) 607–610.
- [44] M. Altarawneh, B.Z. Dlugogorski, E.M. Kennedy, J.C. Mackie, *Prog. Energy Combust. Sci.* 35 (2009) 245–274.
- [45] S. Nganai, S.M. Lomnicki, B. Dellinger, *Environ. Sci. Technol.* 45 (2010) 1034–1040.
- [46] Y. Fan, X. Lu, Y. Ni, H. Zhang, M. Zhu, Y. Li, J. Chen, *Appl. Catal. B: Environ.* 101 (2011) 606–612.



- [47] NIST, X-ray Photoelectron Spectroscopy Database, 2012, <http://srdata.nist.gov/xps/>
- [48] M.W.M. Hisham, S.W. Benson, J. Phys. Chem. 99 (1995) 6194–6198.
- [49] A.P. Amrute, C. Mondelli, M.A.G. Hevia, J. Perez-Ramirez, ACS Catal. 1 (2011) 583–590.
- [50] D. Qiguang, B. Shuxing, W. Zhengyi, W. Xingyi, L. Guanzhong, Appl. Catal. B: Environ. 126 (2012) 64–75.
- [51] D. Qiguang, B. Shuxing, W. Xingyi, L. Guanzhong, Appl. Catal. B: Environ. 129 (2013) 580–588.